INL/JOU-24-78474-Revision-0

Electronic structure of a nodal line semimetal candidate TbSbTe

June 2025

Iftakhar Bin Elius, Jacob F Casey, Sabin Regmi, Volodymyr Borysovych Buturlim, Anup Pradhan Sakhya, Milo Sprague, Mazharul Islam Mondal, Nathan Valadez, Arun K Kumay, Justin Scrivens, Yenugonda Venkateswara, Shovan Dan, Tetiana Romanova, Arjun K Pathak, Krzysztof Gofryk, Andrzej Ptok, Dariusz Kaczorowski, Madhab Neupane

INL/JOU-24-78474-Revision-0

Electronic structure of a nodal line semimetal candidate TbSbTe

Iftakhar Bin Elius, Jacob F Casey, Sabin Regmi, Volodymyr Borysovych Buturlim, Anup Pradhan Sakhya, Milo Sprague, Mazharul Islam Mondal, Nathan Valadez, Arun K Kumay, Justin Scrivens, Yenugonda Venkateswara, Shovan Dan, Tetiana Romanova, Arjun K Pathak, Krzysztof Gofryk, Andrzej Ptok, Dariusz Kaczorowski, Madhab Neupane

June 2025

Idaho National Laboratory
Idaho Falls, Idaho 83415

http://www.inl.gov

Prepared for the
U.S. Department of Energy
Under DOE Idaho Operations Office
Contract DE-AC07-05ID14517, DE-AC07-05ID14517

Electronic structure of a nodal line semimetal candidate TbSbTe

Iftakhar Bin Elius,[1] Jacob F. Casey,[2] Sabin Regmi,[1,3] Volodymyr Buturlim,[4] Anup Pradhan Sakhya,[1] Milo Sprague,[1]
Mazharul Islam Mondal,[1] Nathan Valadez,[1] Arun K. Kumay,[1] Justin Scrivens,[1] Yenugonda Venkateswara,[2] Shovan Dan,[5]
Tetiana Romanova,[5] Arjun K Pathak,[2] Krzysztof Gofryk,[3] Andrzej Ptok,[6] Dariusz Kaczorowski,[5]
and Madhab Neupane[1,*]

[1]*Department of Physics, University of Central Florida, Orlando, Florida 32816, USA*
[2]*Department of Physics, SUNY Buffalo State, Buffalo, New York 14222, USA*
[3]*Center for Quantum Actinide Science and Technology, Idaho National Laboratory, Idaho Falls, Idaho 83415, USA*
[4]*Glenn T. Seaborg Institute, Idaho National Laboratory, Idaho Falls, Idaho 83415, USA*
[5]*Institute of Low Temperature and Structure Research, Polish Academy of Sciences, ul. Okólna 2, 50-422 Wrocław, Poland*
[6]*Institute of Nuclear Physics, Polish Academy of Sciences, W. E. Radzikowskiego 152, PL-31342 Kraków, Poland*

The LnSbTe (Ln = Lanthanides) family, like isostructural ZrSiS-type compounds, has emerged as a fertile playground for exploring the interaction of electronic correlations and magnetic ordering with the nodal line band topology. Here, we report on a detailed electronic band structure investigation of TbSbTe, corroborated by electrical transport, thermodynamic, and magnetic studies. Temperature-dependent magnetic susceptibility and thermodynamic transport studies indicate the onset of antiferromagnetic ordering below $T_N \sim 5.8\,\mathrm{K}$. The electronic band structure study, carried out with high-resolution angle-resolved photoemission spectroscopy measurements aided with density functional theory–based first-principles calculations reveal presence of a nonsymmorphic symmetry-protected Dirac crossing in the Γ-X high-symmetry (HS) direction, which is part of a nodal line along the X-R HS direction. Another Dirac crossing occurs along the Γ-X direction at a relatively higher binding energy, which occurs from $\tilde{\mathcal{C}}_{2v}\mathcal{P}$ symmetry which is gapped in the theoretical calculations with the effect of spin-orbit coupling considered. Parallel to this direction, our theoretical calculations and experimental results exhibit strongly momentum-dependent surface bands. In this paper, we open an avenue to further uncover the intricate interplay among symmetry-protected topological band structure, spin-orbit coupling, and magnetism in this material and the LnSbTe family, in general.

I. INTRODUCTION

Since the discovery of topological insulators (TIs), the fascinating field of topological quantum materials (TQMs) has emerged as one of the frontiers of physics [1–4]. Serving as the arena for numerous foundational physical phenomena, these topological materials are continually evolving through robust theoretical and experimental investigations. This evolution has fostered the recognition of a variety of topological semimetals, including but not limited to Dirac [5–9] and Weyl semimetals [10–14], nodal line semimetals (NLSMs) [15–23], and Dirac nodal arcs [24,25]. In a system with both time-reversal symmetry and inversion symmetry, band crossings can lead to the formation of Dirac nodes. At a Dirac node, two doubly degenerate bands touch each other, resulting in a fourfold degenerate crossing point. The linear dispersion relation around the Dirac node leads to massless Dirac fermions as the low-energy excitations in the system. We can classify or differentiate these TQMs based on the dimensionality of their band interactions or crossings in the momentum space [6,8]. The idea of zero-dimensional band contact points in Dirac or Weyl semimetals is further extended to higher-dimensional nodal lines or surfaces [15,17,26]. In NLSMs, the band interactions extend in the form of lines or closed loops, which are protected by extra symmetries like mirror reflection, inversion, time-reversal, spin-rotation, or nonsymmorphic symmetries [15,17,18,27]. Nonsymmorphic symmetry incorporates a point group operation like fractional lattice translation with a nonprimitive lattice translation like screw axis or glide operation [28]. The pursuit of nonsymmorphic topological materials has been largely navigated by the seminal research throughout the last few years, yet the number of material families featuring nonaccidental nodal lines bereft of spin-orbit coupling (SOC) is significantly limited [18,29–32]. Authors of some of the recent studies have elucidated the possibility of continuous Dirac nodal points, under the condition that two-dimensional (2D) square motifs twisted into hosting a unit cell, leading to a glide symmetry [29,30]. These theoretical speculations came into existence since such nodal line topological phases were observed in ZrSiS followed by other MZX (M = transition elements; Z = Si, Ge, Sb, and Sn; and X = S, Se, and Te) materials with PbFCl-type crystal structure [17,18]. When the transition metals are replaced by rare-earth elements, different topological properties can be expected due to the correlations between $4f$ and conduction band electrons and magnetism inherent to $4f$ states within the LnSbTe family. GdSbTe,

---

[*] madhab.neupane@ucf.edu

one of the materials reported from this family, has ZrSiS-like nodal line characteristics, translated into energy positions [33]. In HoSbTe, an SOC gap opening was experimentally observed at the X point [34,35], turning it into a promising material for a weak TI. Also, its band structure has been reported to show magnetism-driven changes upon antiferromagnetic (AFM)-to-ferromagnetic (FM) transition ∼4 K [34]. Similar metamagnetic transitions [36], charge density wave (CDW) state and weak Kondo effect, were observed in CeSbTe [36–38]. In LaSbTe, at least two nodal lines along the X-R and A-M directions were found to be robust against SOC protected by the nonsymmorphic symmetry [39,40]. Authors of angle-resolved photoemission spectroscopy (ARPES) studies on NdSbTe revealed two nodal lines along R-X and one diamond-shaped nodal line structure around the Γ point as well as bands forming nodal lines along the Γ-M direction [41]. Authors of a magnetic and electronic study on NdSbTe revealed characteristic metamagnetic transitions in the AFM region (below $T_N \sim 2.7$ K), Kondo localization, and enhanced electronic correlation [42]. Authors of experimental studies on SmSbTe showed multiple Dirac nodes which are part of nodal lines along the Γ-X and X-R high-symmetry (HS) directions [43,44]. Very recently, authors of ARPES-based studies on PrSbTe revealed similar electronic structure with gapless nodal line features [45] . The terbium variant of this series TbSbTe remains underexplored with respect to the employment of experimental methodologies for the simultaneous investigation of its electronic structure and its electrical, magnetic, and thermodynamic properties. A preceding analysis utilizing neutron diffraction methods on TbSbTe brought to light the existence of competing magnetic phases within the AFM state [46]. Complementary to this, authors of another study on TbSbTe presented an amalgamation of thermodynamic, magnetic, and electronic transport measurements, supplemented by theoretical computations of the electronic band structure [47]. Notwithstanding these contributions, an experimental exploration of the electronic band structure of TbSbTe via ARPES with comprehensive integration with thermodynamic, electronic, and magnetic measurements to scrutinize the nodal line attributes of this variant remains unreported. This advancement is poised to significantly enrich our understanding of the unique quantum properties of this lesser-studied compound.

In this paper, we present thermodynamic, magnetic, electrical transport, and magnetoresistive studies of the TbSbTe single crystals. To investigate the electronic band structure of the material, we performed our electronic band structure studies on TbSbTe via ARPES, corroborated with the first-principles calculations. The ARPES measurements were carried out at the paramagnetic (PM) phase (at 18 K), which harbors persistent nodal-line-like features along several HS directions. Within the resolution of the ARPES spectra, we observe gapless band crossings along the $\overline{\Gamma}$-$\overline{X}$ and $\overline{\Gamma}$-$\overline{M}$ directions that form a nodal line along the bulk X-R line and a diamond shape centered at the $\overline{\Gamma}$ point in the k_x-k_y plane, respectively. In this paper, we provide key insights into the electronic structure and topological states of TbSbTe, introducing a valuable foundation for understanding the topological properties of the LnSbTe family.

II. METHODS

High-quality single crystals of TbSbTe were grown using the self-flux method. The reactants were mixed in a stoichiometric composition and placed in an alumina crucible and then sealed in a quartz ampule in vacuum. The ampule was then placed in a muffle furnace and heated to 1000 °C at a rate of 10 °C/h. The temperature was held there for 10 h and then cooled to 600 °C at a rate of 2 °C/h, then excess Sb flux was separated using a centrifuge followed by a natural cooling of the sample. The chemical composition and phase purity of the crystals were ascertained through energy-dispersive x-ray (EDX) analysis, conducted using a FEI scanning electron microscope outfitted with an EDAX Genesis XM4 spectrometer. Furthermore, the crystal structure was validated by powder x-ray diffraction (XRD) analysis, performed on finely ground polycrystals of TbSbTe using a PANalytical X'pert Pro diffractometer equipped with Cu-$K\alpha$ radiation. The orientation of the crystals selected for physical properties measurements was determined by means of backscattered Laue diffraction, carried out on a Proto Manufacturing Laue-COS camera. The calculated crystal structure was visualized using the software VESTA version 3 [48], and the three-dimensional (3D) Brillouin zone [BZ; in the inset of Fig. 1(b)] was generated using the software XCrySDen version 1.6.2 [49].

Magnetic measurements were carried out in the temperature interval 2–300 K in magnetic fields up to 14 T using a Quantum Design DynaCool-14 Physical Property Measurement System (PPMS). The heat capacity was measured from 1.72 to 210 K, employing a relaxation technique and two-τ model implemented in the PPMS platform.

Electrical transport measurements were performed in a thin bar-shaped piece of crystal (cross-section: $244.5 \times 155.5\ \mu\text{m}^2$, and distance between voltage probe: 644.5 μm) using a commercial PPMS platform. The magnetoresistance (MR) data have been symmetrized to eliminate possible contribution from the Hall resistance. The thermodynamic and electrical transport measurements were plotted using the OriginPRO (version 2016a) software package developed by Origin Lab.

The electronic band structure measurements were performed on a high energy resolution spectrometer (HERS) ARPES at the Advanced Light Source (ALS) beamline end station 10.0.1.1. The energy resolution was set to be better than 20 meV, and the angular resolution was better than 0.2° for all measurements [50]. The samples were mounted on copper sample holders. Then posts were attached to their upper surface using silver epoxy. Then they were transferred to the high-vacuum ARPES chamber and cleaved *in situ* at a pressure better than 10^{-10} Torr, and measurements were performed at a temperature of 18 K. All ARPES data presented in this paper and the Supplemental Material (SM) [51] were analyzed using the Igor pro 8.0.4 software package developed by WaveMetrics.

The *ab initio* calculations based on density functional theory (DFT) were performed using the projector augmented-wave potentials [52] implemented in the VASP code [53–55]. Calculations are made within the generalized gradient approximation in the Perdew, Burke, and Ernzerhof parametrization

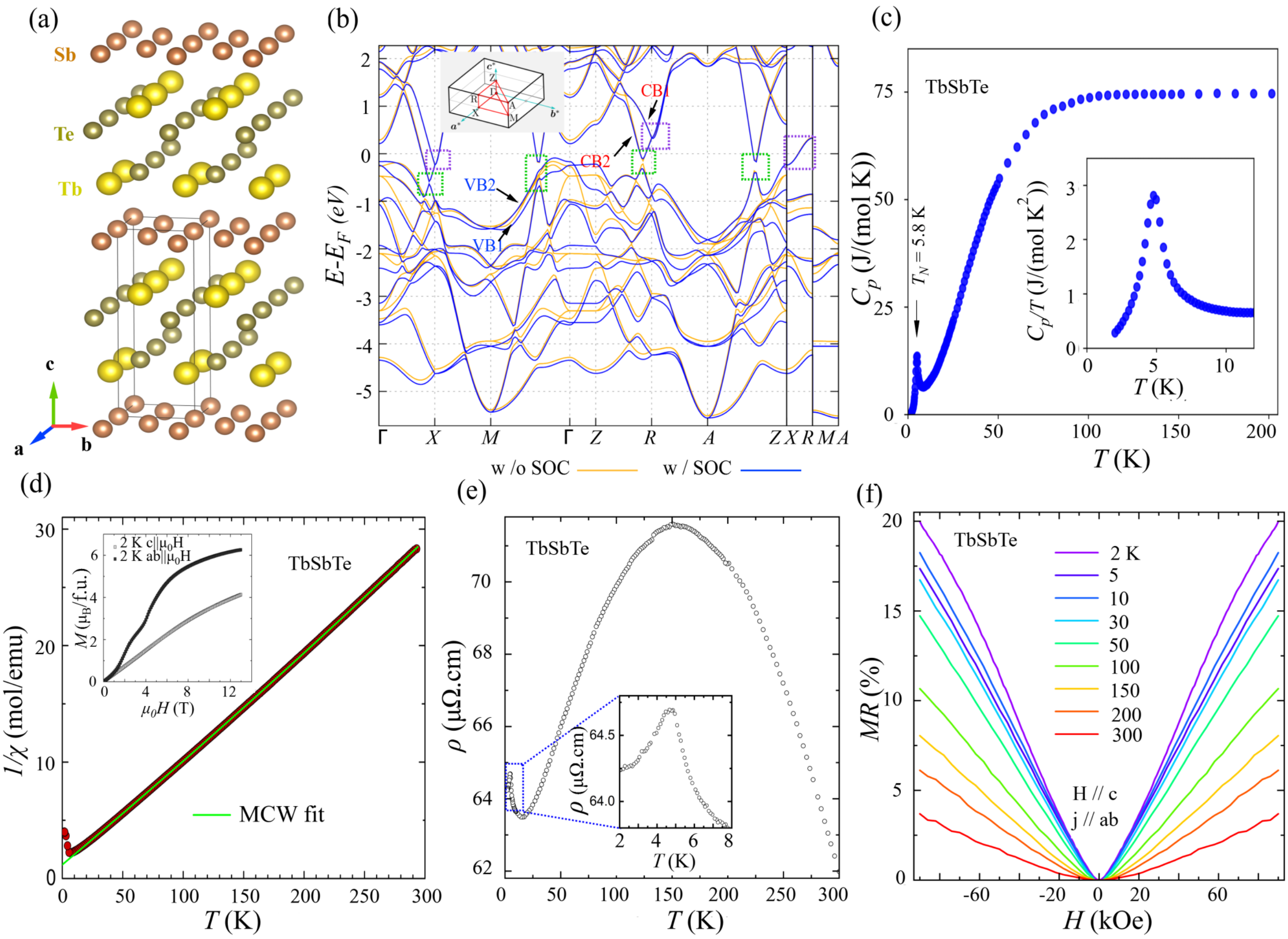

FIG. 1. Crystal structure, electronic band structure, thermodynamic, magnetic, and transport properties of TbSbTe. (a) Crystal structure of TbSbTe; two zigzag chains of Tb-Te are sandwiched by square planar two-dimensional (2D) Sb nets. (b) Calculated band structure in paramagnetic (PM) phase, without considering spin-orbit coupling (SOC; yellow) and with consideration of SOC (blue). The positions of the nodal lines (which correspond to the experimental observations) are marked with green boxes. The result corresponds to calculations where the f states were treated as core states. (c) Temperature dependence of specific heat of TbSbTe; the black arrow indicates the antiferromagnetic (AFM)-to-PM phase transition, and the C_p/T vs T curve zoomed in at the low-temperature range is presented in the inset. (d) Temperature dependence of the inverse dc susceptibility χ^{-1}, measured in a magnetic field of $\mu_0 H = 0.5$ T. The solid green line represents the modified Curie-Weiss fit to the experimental data >30 K. [Inset: Magnetization isotherms measured at 2 K with the magnetic field applied parallel to the ab plane (solid squares) and the c axis (open squares)]. (e) Temperature dependence of electrical resistivity (Inset: A magnified view at low-temperature range showing AFM-to-PM transition). (f) Magnetoresistance (MR) measured in different temperatures from 2 to 300 K.

[56]. The energy cutoff for the plane-wave expansion was set to 300 eV, while f electrons were treated as core states. In the case of magnetic calculations (with f electrons treated as valence states), we assumed an AFM configuration and applied a Hubbard $U = 6$ eV within the Dudarev approach [57]. Optimizations of structural parameters (lattice constants and atomic positions) were performed in the primitive unit cell using the $15 \times 15 \times 15$ k-point grid in the Monkhorst-Pack scheme [58]. As a break of the optimization loop, we take the condition with an energy difference of 10^{-6} and 10^{-8} eV for ionic and electronic degrees of freedom. The topological properties as well as the electronic surface states were studied using the tight-binding model in the maximally localized Wannier orbitals basis [59–61]. This model was constructed from exact DFT calculations in a primitive unit cell (containing 1 f.u.), with $10 \times 10 \times 6$ Γ-centered k-point grid, using the WANNIER90 software [62]. During the calculations, the f electrons of Tb were treated as a core state. The electronic surface states were calculated using the surface Green's function technique for a semi-infinite system [63], implemented in WANNIERTOOLS [64].

III. RESULTS

A. Crystal and electronic structure

Like other LnSbTe materials, TbSbTe also crystallizes in the tetragonal $P4/nmm$ space group (No. 129) having the unit cell parameters $a = b = 4.25$ Å and $c = 9.212$ Å [47]. The atoms are located in the HS Wyckoff positions with Tb at $(2c)$ position: $(\frac{1}{4}, \frac{1}{4}, 0.2759)$, Sb at $(2a)$ position: $(\frac{3}{4}, \frac{1}{4}, 0)$, and Te at $(2c)$ position: $(\frac{1}{4}, \frac{1}{4}, 0.6244)$ [46,47,65] (Laue XRD pattern and EDX spectra are presented in Fig. S1 in the SM [51]). The crystal structure of TbSbTe presented in Fig. 1(a) comprises stacking of two Te-Tb-Te-Tb zigzag slabs having a $(\frac{1}{2}, \frac{1}{2}, z)$ shift relative to each other that sandwich each square-planar Sb net when viewed along the c axis [46] (see Figs. S2(a)–S2(c) in the SM [51]).

The BZ, its 2D projection onto the (001) plane, and the positions of the nodal lines (along with the symmetries protecting them) are presented in Fig. S2(d) in the SM [51]. Figure 1(b) displays the calculated bulk band structure with (blue bands) and without (yellow bands) the effect of SOC, in the PM phase. The locations corresponding to the nodal points observed in the experimental findings are indicated with green boxes. The nodal points can be tracked along the k_z plane to the parallel HS directions to perceive their inclusion in a continuum of intersections. The bands of interest, taking part in formation of the nodal line features, are marked with CB1, CB2, VB1, and VB2 in Fig. 1(b). Schematics for better understanding the nodal features are added in Figs. S2(e) and S2(f) in the SM [51]. The bulk band structures in both the nonmagnetic and AFM phases, calculated with enhanced momentum resolution, are presented in Fig. S3 in the SM [51]. The numerically obtained nodal lines, originating from these band crossings, are presented in Fig. S4 in the SM [51]. In addition to the symmetry-enforced nodal lines along the X-R and M-A directions, several accidental band crossings are also observed along the BZ boundaries.

B. Bulk thermodynamic and electronic transport properties

The heat capacity data presented in Fig. 1(c) corroborates the AFM order in TbSbTe. The AFM phase transition manifests itself as a distinct λ-type anomaly in $C_p(T)$, the position of which perfectly coincides with T_N determined from the magnetic data. Above ∼100 K, $C_p(T)$ saturates at a value of 75.7 J/mol K that is very close to the Dulong-Petit limit $3nR = 74.79$ J/mol K ($n = 3$ is the number of atoms per formula unit, and R stands for the gas constant). It should be noted that this finding notably differs from the results published before [47]. Here, it should also be emphasized that the quantitative analysis of $C_p(T)$ of TbSbTe, either within the framework of the simplified Debye model ($C \sim T^3$) or full Debye or Debye-Einstein formulas, is difficult without knowing the Schottky contribution from crystalline electric field excitations, which cannot be neglected at temperatures $T > 6$ K. In contrast, $C_p(T)$ in the AFM region is likely dominated by magnon contribution, which may be complex in nature, as suggested by the neutron diffraction results indicating the presence below T_N of several competing commensurate and incommensurate magnetic orderings [46].

Figure 1(d) shows the temperature dependence of the inverse magnetic susceptibility (where $\chi \equiv M/H$) of TbSbTe measured in a magnetic field applied along the crystallographic c axis. In agreement with the previous reports [46,47], $\chi(T)$ shows a sharp maximum, marking the transition from PM to AFM state. The Néel temperature derived from this data is 5.8 K; that is lower than $T_N = 6.4$ K given in Ref. [46], yet fairly close to $T_N = 6.0$ K determined in Ref. [47]. As can be inferred from Fig. 1(d), in the PM state, $\chi(T)$ can be approximated by the modified Curie-Weiss (MCW) law $\chi(T) = \chi_o + \frac{C}{(T-\theta_p)}$, with the parameters $\chi_o = -2.4 \times 10^{-3}$ emu/mol, $C = 11.6$ emu K/mol, and $\theta_p = -13.7$ K. The term χ_o is the sum of all the temperature-independent contributions to the magnetic susceptibility due to conduction electrons, core electrons, polarization effects, and crystal electric field effect. The effective magnetic moment μ_{eff}, calculated from the value of the Curie constant C, equals 9.61 μ_B/f.u., which is very close to the theoretical prediction for free Tb^{3+} ion (9.72 μ_B). The negative sign of the PM Curie temperature θ_p signals the predominance of AFM exchange interactions, in line with the AFM character of the electronic ground state in TbSbTe. It is worth noting that the values of μ_{eff} and θ_p are in good agreement with those reported in Ref. [47], $\mu_{\text{eff}} = 9.76$ and $\theta_p = -12$ K for $H \parallel ab$. In Ref. [46], a polycrystal was measured so no direct comparison is justified in the case of a highly anisotropic material like TbSbTe.

The inset of Fig. 1(d) shows the magnetization $M(H)$ in TbSbTe measured at $T = 2$ K in external magnetic field parallel to the c axis (hard axis) and the ab crystallographic basal plane (easy axis). In agreement with the results shown in Ref. [47], the isotherm (with $\mu_0 H \parallel ab$) exhibits two inflection points of metamagneticlike character. The occurrence of multistep changes in $M(H)$ can be associated with a complex noncollinear magnetic structure in zero magnetic field that at $T = 2$ K is defined by two propagation vectors $\mathbf{k}_1 = (\frac{1}{2}\ 0\ 0)$ and $\mathbf{k}_2 = (\frac{1}{2}\ 0\ \frac{1}{4})$ [46]. It is known that multi-k spin structures are susceptible to external magnetic field which often results in multiple field-induced rearrangements.

The temperature dependence of the electrical resistivity $\rho(T)$ measured within the tetragonal plane of TbSbTe is shown in Fig. 1(e). Both the magnitude and the shape of $\rho(T)$ reflect the semimetallic character of the compound. The $\rho(T)$ curve features a broad hump ∼150 K, which may be associated with the interplay of gradual damping in charge-carrier concentration and increase in scattering cross-section, both occurring with decreasing temperature [35,46,47,66]. Another feature in $\rho(T)$ is an upturn in the vicinity of T_N followed by a sharp peak ∼5 K [see the inset to Fig. 1(e)] that manifests the onset of the ordered state. In the prior study, a broad hump in $\rho(T)$ was revealed, occurring ∼240 K; however, no clear anomaly at T_N was detected. The difference in the hump position may be attributed to diverse carrier concentrations in the crystals investigated. It seems likely that the same factor is responsible for the dissimilarities observed near T_N.

The transverse $\text{MR} = [\rho(H)/\rho(0) - 1] \times 100$ of TbSbTe was measured with electric current flowing in the basal plane and magnetic field directed along the tetragonal c axis at several temperatures below and above T_N [see Fig. 1(f)]. At 2 K, MR reaches 9 T, a value of 20%, which quantitatively agrees with the previous study [47].

C. Observation of nodal line states

To reveal the electronic structure of the compound, the Fermi surface (FS) map along with its second derivative (SD), collected at 60 eV incident photon energy, are presented in the top panel of Figs. 2(a) and 2(b), respectively. As can be inferred from Fig. 2(c), the experimental ARPES data can be very well reproduced in the calculations based on DFT [presented in Figs. 2(h)–2(k)]. At the k_x-k_y plane, the FS consists of two diamond-shaped isocentric (around the Γ point) sheets. Examination of the constant energy contours (CECs) at

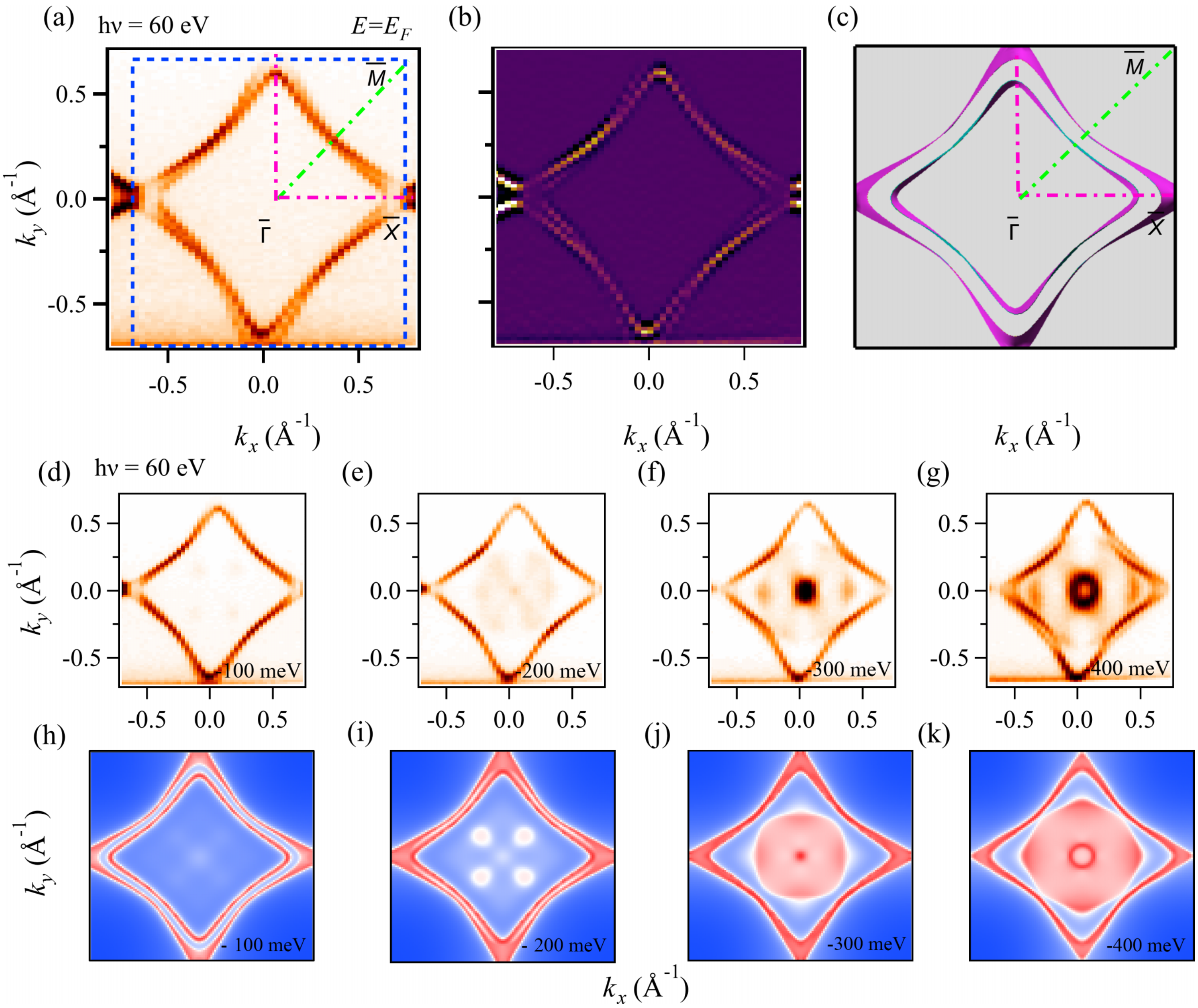

FIG. 2. Fermi surface (FS) and constant energy contour (CEC) maps of TbSbTe. (a) Experimentally observed FS map of TbSbTe at an incident photon energy of 60 eV; the surface Brillouin zone is marked with a blue-dashed square, and all the high-symmetry (HS) points ($\overline{\Gamma}$, $\overline{M}$ and $\overline{X}$) are marked. (b) Second derivative (SD) of the experimental FS. (c) FS obtained from density functional theory (DFT)-based calculations with the inclusion of spin-orbit coupling (SOC). (d)–(g) Experimentally observed CEC maps at 100, 200, 300, and 400 meV below the FS, (h)–(k) theoretically calculated CECs, with their binding energies marked on each of the contour plots. The angle-resolved photoemission spectroscopy (ARPES) measurements were done at the Advanced Light Source (ALS) beamline 10.0.1.1 at a temperature of 18 K.

higher binding energies [see Figs. 2(d)–2(g)] below the Fermi level indicates convergence of the two-sheeted diamondlike structure into a singular sheet. This coalesced single sheet retains the single-sheet character until 300 meV of binding energy. However, ∼500–600 meV (see CECs measured at higher binding energy presented in Fig. S5 in the SM [51]. FS and CECs measured at different incident photon energies are also presented in Fig. S6 in the SM [51]) [51], the layers gradually diverge and revert to their dual-layer nature (for detailed analysis see Fig. S7 in the SM [51]).

To better understand the band crossings in the band structure of TbSbTe, we investigated the ARPES dispersion maps along different HS directions ($\overline{\Gamma}$-$\overline{X}$, $\overline{\Gamma}$-$\overline{M}$, and $\overline{X}$-$\overline{M}$). The dispersion maps along $\overline{\Gamma}$-$\overline{X}$ and $\overline{X}$-$\overline{M}$, measured at an incident photon energy of 60 eV, are presented in Figs. 3(a) and 3(d) (dispersion maps at different HS directions measured at other incident photon energies are presented in Fig. S8 in the SM [51]). In Fig. 3(a), along $\overline{X}$-$\overline{\Gamma}$-$\overline{X}$, two distinct crossing points can be observed [marked with green (protected by nonsymmorphic symmetry) and yellow (not protected by nonsymmorphic symmetry) arrows in Fig. 3(b)], which are parts of the nodal lines, a common feature for the isostructural *Ln*SbTe materials [36,39,43]. These features were also reported in recent theoretical studies on TbSbTe as well [47]. The first crossing occurs at the $\overline{X}$ point which can be better observed in the SD plot of the dispersion map presented in Fig. 3(b) (also see Fig. S9 in the SM [51], which presents the dispersion map, its SD, and the momentum dispersion curve at an incident photon energy of 50 eV, to ascertain the presence of the Dirac-like crossing).

The band crossing at the X point remains robust against consideration of SOC, as it is protected by the additional

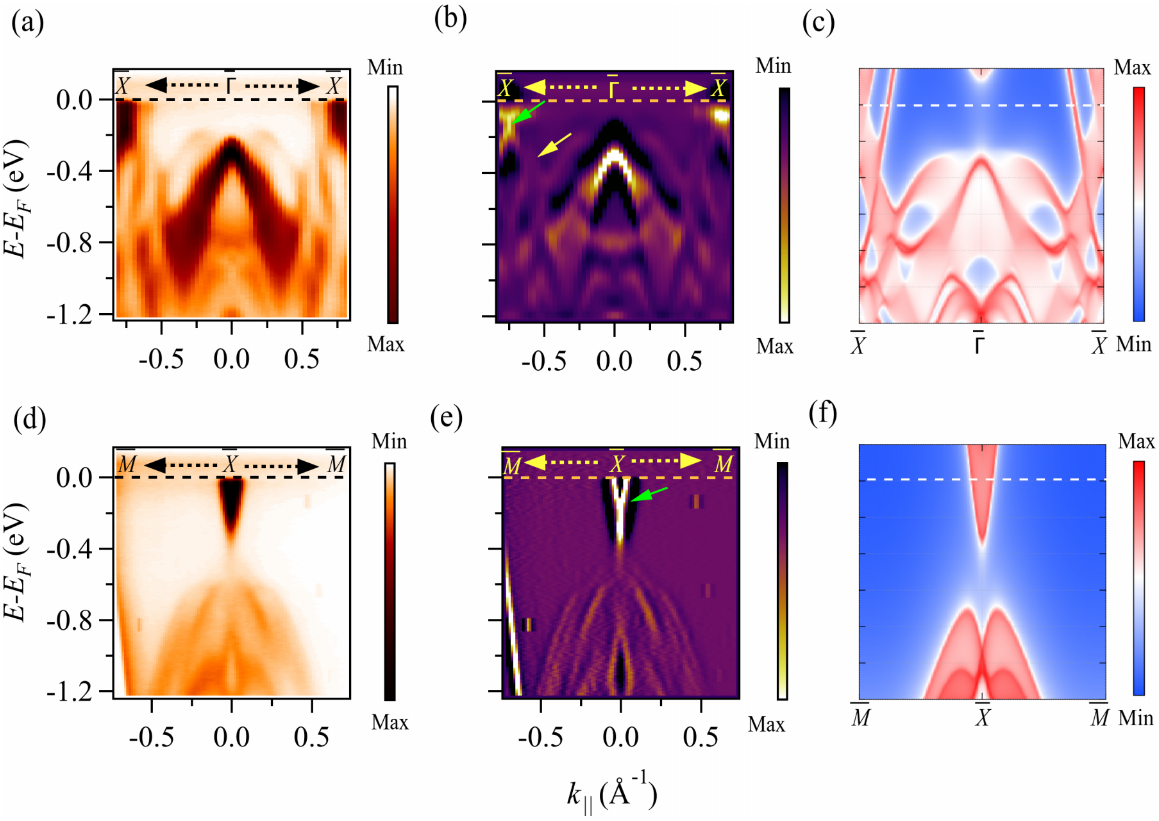

FIG. 3. Observation of nodal line features parallel to the $\overline{X}$-$\overline{\Gamma}$-$\overline{X}$ and $\overline{M}$-$\overline{X}$-$\overline{M}$ directions. (a) Electronic dispersion map along $\overline{X}$-$\overline{\Gamma}$-$\overline{X}$ direction, (b) second derivative (SD) of the dispersion map along $\overline{X}$-$\overline{\Gamma}$-$\overline{X}$, the nodal points which are parts of nodal lines are marked with green (protected by nonsymmorphic symmetry) and yellow (not protected by nonsymmorphic symmetry) arrows, respectively. (c) Theoretically calculated surface projected band structure along $\overline{X}$-$\overline{\Gamma}$-$\overline{X}$. (d) Dispersion maps along $\overline{M}$-$\overline{X}$-$\overline{M}$, (e) their SD, and (f) theoretically calculated surface projected band structure. All the angle-resolved photoemission spectroscopy (ARPES) dispersion maps were collected at beam line 10.0.1.1 at the Advanced Light Source (ALS) at a temperature of 18 K.

nonsymmorphic symmetry, a well-known phenomenon in this system of materials. The experimentally obtained dispersion maps at different incident photon energies, parallel to the Γ-X (or Z-R) direction are presented in Figs. S8(a)–S8(e) in the SM [51], which show the consistent presence of this crossing at the $\overline{X}$ point at all photon energies, suggesting that the crossing is a part of the out-of-plane nodal line along k_z. To better visualize the crossings, SD plots of the dispersion cuts measured with various incident photon energies are presented in Fig. S10 in the SM [51]. The second crossing along the $\overline{\Gamma}$-$\overline{X}$ direction occurs ∼330 meV below the Fermi level. The positions of these Dirac crossings are plotted as a function of incident photon energies in Fig. S11 in the SM [51]. Theoretical calculations suggest the existence of a small gap in the $k_z = 0$ plane, which widens as we move toward the $k_z = \pi$ plane. However, this gap remained indiscernible in any of the dispersion cuts measured with different incident photon energies. Detailed analysis to examine the existence of these gaps is presented in Fig. S12 in the SM [51], exhibiting no signature of discontinuity in the intensity profiles, hinting at the absence of detectable gaps. Next, we move onto the $\overline{M}$-$\overline{X}$-$\overline{M}$ HS direction. Figure 3(d) presents the dispersion cut along $\overline{M}$-$\overline{X}$-$\overline{M}$, its SD, and its theoretically calculated surface spectrum [Figs. 3(e) and 3(f)]. An electronlike pocket is present along this direction (dispersion maps along $\overline{M}$-$\overline{X}$-$\overline{M}$ measured at other photon energies are presented in Figs. S7(k)–S7(o) in the SM [51]), which is characteristic of *Ln*SbTe-type materials [33,41,45]. Both bulk band calculations and surface projected spectrum exhibit similar pocketlike features, suggesting the presence of surface and bulk bands forming the pocket. Proceeding to the dispersion cut along $\overline{M}$-$\overline{\Gamma}$-$\overline{M}$, presented in Fig. 4(a), two linear bands with different velocities converge to form an intersection, which is well reproduced in surface projected calculations presented in Fig. 4(c). Again, contrasting the experimental observations, bulk calculation [Fig. 1(b)] suggests that a gap occurs at the intersection of bands CB2 and VB2 [see Fig. 1(b)], which persists in a reduced form, if SOC is considered. This gap was also beyond the detection limits of the ARPES detector. Another notable aspect is a hole pocketlike feature which can also be seen centering at the Γ (or Z) point in cuts parallel to both Γ-X and Γ-M directions (see Figs. 3 and 4, respectively), throughout all the incident photon energies (presented in Figs. S7(a)–S7(e) and S7(f)–S7(j) in the SM [51], respectively), but its spectral intensity was highly sensitive to the incident photon energy.

D. Momentum dependent surface states parallel to $\overline{\Gamma}$-$\overline{X}$

A detailed analysis of the surface states based on theoretical and experimental results is presented in Fig. 5. The

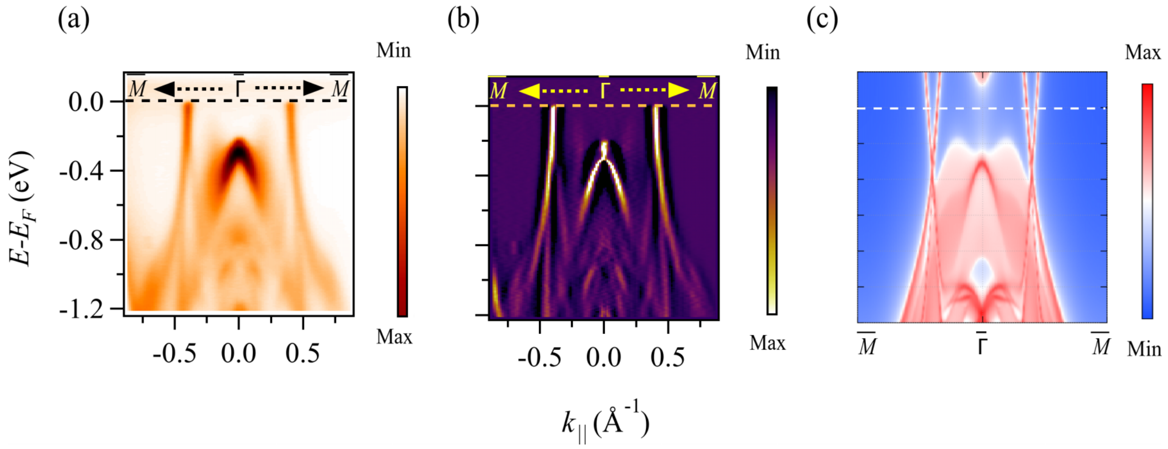

FIG. 4. Observation of nodal states at the $\overline{\mathrm{M}}$-$\overline{\Gamma}$-$\overline{\mathrm{M}}$ direction. (a) Dispersion map along $\overline{\mathrm{M}}$-$\overline{\Gamma}$-$\overline{\mathrm{M}}$ high-symmetry (HS) direction measured with 60 eV incident photon energy at a temperature of 18 K at the Advanced Light Source (ALS) beamline 10.0.1.1. (b) Second derivative of $\overline{\mathrm{M}}$-$\overline{\Gamma}$-$\overline{\mathrm{M}}$ dispersion map, and (c) theoretically calculated surface band map along $\overline{\mathrm{M}}$-$\overline{\Gamma}$-$\overline{\mathrm{M}}$.

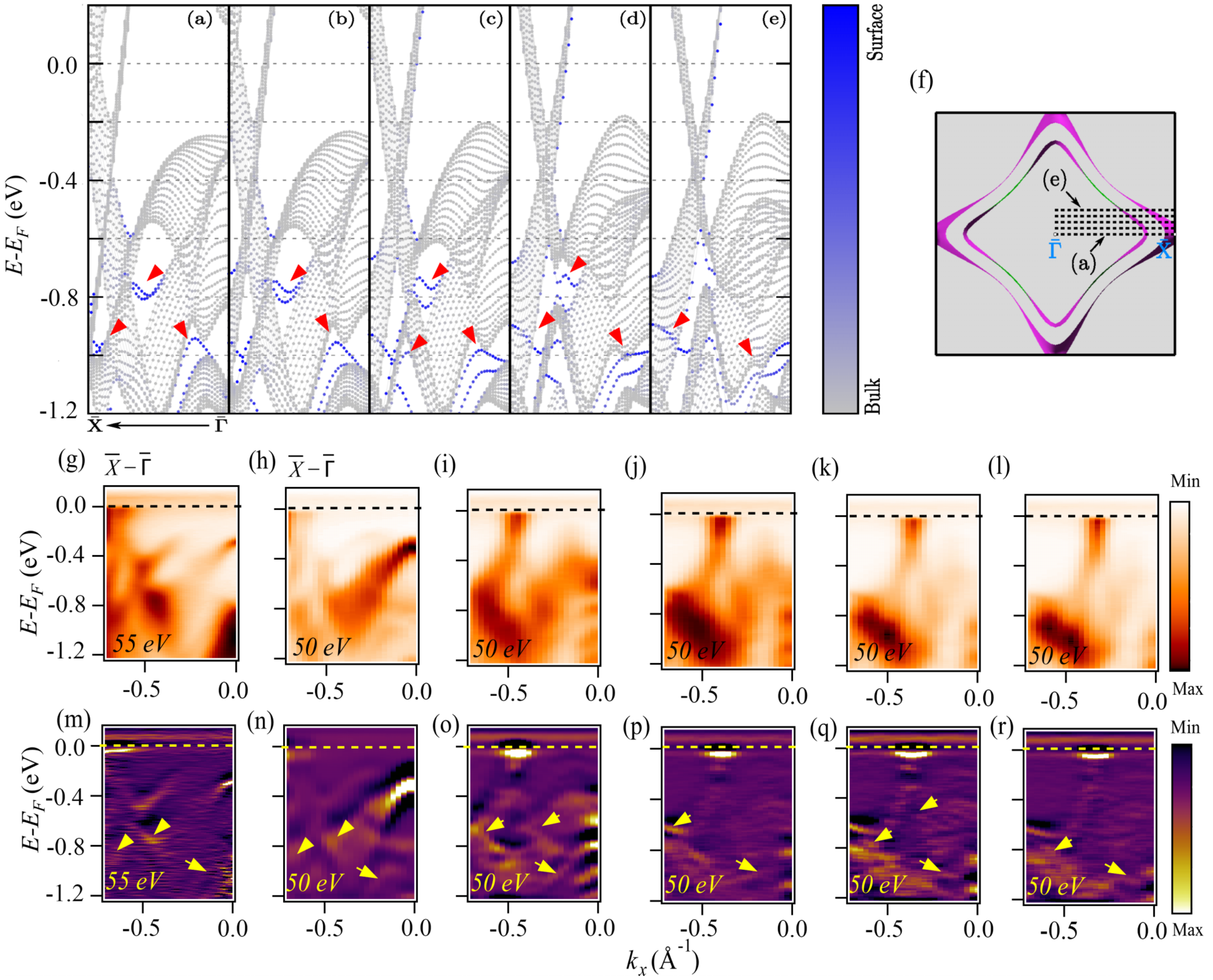

FIG. 5. Surface states parallel to the $\overline{\Gamma}$-$\overline{\mathrm{X}}$ direction. (a)–(e) show the calculated band structures for the slab geometry along cuts presented in (f). The surface originated bands (blue) are marked with red arrows. Angle-resolved photoemission spectroscopy (ARPES) experimental spectra along the $\overline{\Gamma}$-$\overline{\mathrm{X}}$ high-symmetry (HS) direction recorded with (g) 55 eV and (h) 50 eV incident photon energies, and cuts at the corresponding positions of (b)–(e) are presented in (i)–(l). To resolve the band features better, the second derivatives of (g)–(l) are presented in (m)–(r). Here, the surface-originated bands are marked with yellow arrows. The experimental measurements were performed at a temperature of 18 K at the Advanced Light Source (ALS) beamline 10.0.1.1.

theoretically calculated surface Green's function and slab band structures are presented in Figs. 5(a)–5(e), along and parallel to the $\overline{\Gamma}$-$\overline{\text{X}}$ HS direction [see the cuts in the FS map in Fig. 5(f)]. The gray bands corresponds to bulk, and blue bands correspond to surface-originated bands. The band features centering at the Γ and X HS points are predominately bulk originated. The theoretical calculations are well reproduced in the experimental ARPES-based observations presented in Figs. 5(g)–5(l) and their corresponding SDs in Figs. 5(m)–5(r). Figures 5(g) and 5(h) are ARPES dispersion cuts measured with 55 and 50 eV of incident photon energies along $\overline{\Gamma}$-$\overline{\text{X}}$, exhibiting surface bands forming pockets around the $\overline{\Gamma}$ HS point. From E_F to 600 meV binding energy, a linearly dispersing surface band is observed within the bulk bands. Below that, in the proximity of 800 meV binding energy, two branches of surface bands are observed. Another set of surface bands are observed right at the $\overline{\text{X}}$ HS point. In total, we see four regions containing the surface bands. Cuts parallel to $\overline{\Gamma}$-$\overline{\text{X}}$ directions, presented in Figs. 5(h)–5(l) and their corresponding SD plots in Figs. 5(n)–5(r), exhibit strong momentum dependence of the surface bands.

IV. DISCUSSION

Thermodynamic, magnetic, and transport measurements on TbSbTe single crystals coherently exhibit an AFM-to-PM phase transition ~5.8 K. The electronic band structure of TbSbTe, in ARPES spectrographs, exhibits two isocentric diamond-shaped sheets around the Γ point similar to other *Ln*SbTe and ZrSiS-type materials. For TbSbTe, the double sheet is consistently present throughout the FS, unlike heavier members of *Ln*SbTe (for example, HoSbTe [35]), where the bands tend to gap out while radially going toward the $\overline{\Gamma}$-$\overline{\text{M}}$ direction. Another feature of this FS is that the bands are not as well separated as in NdSbTe [41] or PrSbTe [45,67] nor coalesced into a single sheet like GdSbTe [33]. The features of the nodal line observed in the cuts parallel to $\overline{\Gamma}$-$\overline{\text{X}}$ are well reproduced in bulk electronic calculations. In space group $P4/nmm$, symmetries in combination with nonsymmorphic symmetry play a crucial role in realizing enforced degeneracy in the vicinity of Fermi energy. This space group hosts a glide plane $\tilde{\mathcal{M}}_z = \{\mathcal{M}_z|\frac{1}{2}\frac{1}{2}0\}$, screw axes $\tilde{C}_{2\nu,\,(\nu=x,y)} = \{\mathcal{C}_{2x}|\frac{1}{2}00\}$ and $\{\tilde{\mathcal{C}}_{2y}|0\frac{1}{2}0\}$, mirror symmetries $\tilde{\mathcal{M}}_x = \{\mathcal{M}_x|\frac{1}{2}00\}$, $\tilde{\mathcal{M}}_y = \{\mathcal{M}_y|0\frac{1}{2}0\}$, and $\tilde{\mathcal{M}}_{xy} = \{\mathcal{M}_{xy}|\frac{1}{2}\frac{1}{2}0\}$, and the spatial inversion symmetry $\mathcal{P} = \{\mathcal{P}|000\}$. Dirac crossings observed in the HS directions parallel to Γ-X (with different incident photon energies, i.e., at different k_z locations), right at the $\overline{\text{X}}$ points, are degeneracies enforced by the combined effect of glide plane $\tilde{\mathcal{M}}_z$ and time-reversal symmetry $\mathcal{T}$. These crossings are part of the nodal line that extends along the X-R HS direction. The combination of these symmetries ensures the robustness of this nodal line even under consideration of the effect of SOC. The screw axis symmetries $\tilde{C}_{2\nu}$ in conjugation with the inversion symmetry $\mathcal{P}$ allow the other crossing (at the relatively higher energies), which also extends longitudinally along the k_z axis. Mirror symmetry $\tilde{\mathcal{M}}_{xy}$ allows the crossings in the Γ-M HS direction, which are parts of the nodal line extending parallel to the M-A direction, often observed in the ZrSiS-type systems. However, nodes in this direction were not observed conclusively in this paper. Although, except for the nonsymmorphic symmetry enforced nodal line (along X-R, at the X point), consideration of SOC destabilizes the other nodal crossings. Despite the theoretical predictions of destabilized nodal line features, in experimental observations, the nodal lines remain ungapped. This phenomenon could potentially be ascribed to constrained k_z resolution within the vacuum ultraviolet region, resulting in the energy cuts encompassing a spectrum of k_z values rather than being confined to a specific k_z value. An alternate explanation might stem from the prevalent incongruity between experimental results and theoretical predictions often observed in $4f$ systems. Moreover, while the previously discussed symmetries preserve the degeneracies in the PM phase, consideration of magnetic ordering (i.e., AFM or FM magnetic ordering) usually leads to breaking of these degeneracies. In the electrical and thermodynamic measurements, TbSbTe undergoes a PM-to-AFM phase transition; thus, we restrict our considerations to AFM ordering. AFM spin orientation of Tb along the (001) direction elongates the c lattice parameter into $2c$ (technically space group $P4/ncc$ with $\mathcal{T}$). This still guarantees the nodal line along the X-R direction. A similar analysis was also performed in Ref. [30].

V. CONCLUSIONS

To summarize, we present temperature- and magnetic field–dependent thermodynamic and electric transport investigations, which consistently indicate an AFM-to-PM transition at $T_N = 5.8$ K. Concurrently, we studied the electronic band structure of a member of the *Ln*SbTe family TbSbTe using high-resolution ARPES combined with theoretical first-principles calculations. Our electronic structure study revealed multiple band intersections, including a Dirac crossing, formed by bulk bands, in the Γ-X HS direction, which is part of a nodal line extending along the X-R bulk direction. This crossing remains ungapped over k_z, as established in both our theoretical work considering the effect of SOC and our experimental ARPES-based observations. Another Dirac-like crossing in this direction was gapped in the theoretical calculations. These results implicate TbSbTe as a promising candidate for examining the interaction of symmetry, topology, and SOC in the *Ln*SbTe series of materials.

ACKNOWLEDGMENTS

M.N. acknowledges support from the National Science Foundation under the CAREER Award No. DMR-1847962 and the Air Force Office of Scientific Research for MURI Grant No. FA9550-20-1-0322. N.V. acknowledges the support from the Mathematical and Physical Sciences (MPS) Alliances for Graduate Education and the Professoriate—Graduate Research Supplements. D.K. and T.R. were supported by the National Science Centre (Poland) under Research Grant No. 2021/41/B/ST3/01141. V.B. and S.R. acknowledge the support from Idaho National Laboratory's Laboratory Directed Research and Development program under the Department of Energy (DOE) Idaho Operations Office Contract No. DEAC07-05ID14517. K.G. acknowledges support from the Division of Materials Science and Engineering, Office of Basic Energy Sciences, Office of

Science of the DOE. A.P. acknowledges the support by National Science Centre (NCN, Poland) under Project No. 2021/43/B/ST3/02166. In this research, we utilized resources of the Advanced Light Source (ALS) at the Lawrence Berkeley National Laboratory, which is a DOE Office of Science User Facility under Contract No. DE-AC02-05CH11231. Magnetic measurements were performed at the State University of New York, Buffalo State, and supported by the National Science Foundation, Launching Early-Career Academic Pathways in the MPS program under Award No. DMR-2213412. We express our gratitude to Dr. Sung-Kwan Mo for providing valuable support with the beamline at the ALS.

---

[1] M. Z. Hasan and C. L. Kane, Colloquium: Topological insulators, Rev. Mod. Phys. **82**, 3045 (2010).

[2] X.-L. Qi and S.-C. Zhang. Topological insulators and superconductors, Rev. Mod. Phys. **83**, 1057 (2011).

[3] M. Z. Hasan, S.-Y. Xu, and M. Neupane, Topological insulators, topological Dirac semimetals, topological crystalline insulators, and topological Kondo insulators, in *Topological Insulators: Fundamentals and Perspectives*, edited by F. Ortmann, S. Roche, and S. O. Valenzuela (John Wiley & Sons, New York, 2015), pp. 55–100.

[4] M. Sato and Y. Ando, Topological superconductors: A review, Rep. Prog. Phys. **80**, 076501 (2017).

[5] Z. Wang, Y. Sun, X.-Q. Chen, C. Franchini, G. Xu, H. Weng, X. Dai, and Z. Fang, Dirac semimetal and topological phase transitions in A_3Bi ($A =$ Na, K, Rb), Phys. Rev. B **85**, 195320 (2012).

[6] Z. Wang, H. Weng, Q. Wu, X. Dai, and Z. Fang, Three-dimensional Dirac semimetal and quantum transport in Cd_3As_2, Phys. Rev. B **88**, 125427 (2013).

[7] M. Neupane, S.-Y. Xu, R. Sankar, N. Alidoust, G. Bian, C. Liu, I. Belopolski, T.-R. Chang, H.-T. Jeng, H. Lin *et al*., Observation of a three-dimensional topological Dirac semimetal phase in high-mobility Cd_3As_2, Nat. Commun. **5**, 3786 (2014).

[8] Z. K. Liu, B. Zhou, Y. Zhang, Z. J. Wang, H. M. Weng, D. Prabhakaran, S.-K. Mo, Z. X. Shen, Z. Fang, X. Dai *et al*., Discovery of a three-dimensional topological Dirac semimetal Na_3Bi, Science **343**, 864 (2014).

[9] B.-J. Yang and N. Nagaosa, Classification of stable three-dimensional Dirac semimetals with nontrivial topology, Nat. Commun. **5**, 4898 (2014).

[10] S.-Y. Xu *et al*., Discovery of a Weyl fermion semimetal and topological Fermi arcs, Science **349**, 613 (2015).

[11] B. Q. Lv, H. M. Weng, B. B. Fu, X. P. Wang, H. Miao, J. Ma, P. Richard, X. C. Huang, L. X. Zhao, G. F. Chen *et al*., Experimental discovery of Weyl semimetal TaAs, Phys. Rev. X **5**, 031013 (2015).

[12] A. A. Soluyanov, D. Gresch, Z. Wang, Q. Wu, M. Troyer, X. Dai, and B. A. Bernevig, Type-II Weyl semimetals, Nature (London) **527**, 495 (2015).

[13] B. Yan and C. Felser, Topological materials: Weyl semimetals, Annu. Rev. Condens. Matter Phys. **8**, 337 (2017).

[14] A. P. Sakhya, C.-Y. Huang, G. Dhakal, X.-J. Gao, S. Regmi, B. Wang, W. Wen, R.-H. He, X. Yao, R. Smith *et al*., Observation of Fermi arcs and Weyl nodes in a noncentrosymmetric magnetic Weyl semimetal, Phys. Rev. Mater. **7**, L051202 (2023).

[15] C. Fang, Y. Chen, H.-Y. Kee, and L. Fu, Topological nodal line semimetals with and without spin-orbital coupling, Phys. Rev. B **92**, 081201(R) (2015).

[16] Q.-F. Liang, J. Zhou, R. Yu, Z. Wang, and H. Weng, Node-surface and node-line fermions from nonsymmorphic lattice symmetries, Phys. Rev. B **93**, 085427 (2016).

[17] M. Neupane, I. Belopolski, M. M. Hosen, D. S. Sanchez, R. Sankar, M. Szlawska, S.-Y. Xu, K. Dimitri, N. Dhakal, P. Maldonado *et al*., Observation of topological nodal fermion semimetal phase in ZrSiS, Phys. Rev. B **93**, 201104(R) (2016).

[18] L. M. Schoop, M. N. Ali, C. Straßer, A. Topp, A. Varykhalov, D. Marchenko, V. Duppel, S. S. Parkin, B. V. Lotsch, and C. R. Ast, Dirac cone protected by non-symmorphic symmetry and three-dimensional Dirac line node in ZrSiS, Nat. Commun. **7**, 11696 (2016).

[19] G. Bian, T.-R. Chang, R. Sankar, S.-Y. Xu, H. Zheng, T. Neupert, C.-K. Chiu, S.-M. Huang, G. Chang, and I. Belopolski, Topological nodal-line fermions in spin-orbit metal $PbTaSe_2$, Nat. Commun. **7**, 10556 (2016).

[20] M. M. Hosen, K. Dimitri, I. Belopolski, P. Maldonado, R. Sankar, N. Dhakal, G. Dhakal, T. Cole, P. M. Oppeneer, D. Kaczorowski *et al*., Tunability of the topological nodal-line semimetal phase in ZrSiX-type materials ($X =$ S, Se, Te), Phys. Rev. B **95**, 161101(R) (2017).

[21] S. Li, Y. Liu, B. Fu, Z.-M. Yu, S. A. Yang, and Y. Yao, Almost ideal nodal-loop semimetal in monoclinic $CuTeO_3$ material, Phys. Rev. B **97**, 245148 (2018).

[22] N. P. Armitage, E. J. Mele, and A. Vishwanath, Weyl and Dirac semimetals in three-dimensional solids, Rev. Mod. Phys. **90**, 015001 (2018).

[23] J. Zhan, J. Li, W. Shi, X.-Q. Chen, and Y. Sun, Coexistence of Weyl semimetal and Weyl nodal loop semimetal phases in a collinear antiferromagnet, Phys. Rev. B **107**, 224402 (2023).

[24] Y. Wu, L.-L. Wang, E. Mun, D. D. Johnson, D. Mou, L. Huang, Y. Lee, S. L. Bud'ko, P. C. Canfield, and A. Kaminski, Dirac node arcs in $PtSn_4$, Nat. Phys. **12**, 667 (2016).

[25] G. Dhakal, F. Kabir, A. K. Nandy, A. Aperis, A. P. Sakhya, S. Pradhan, K. Dimitri, C. Sims, S. Regmi, M. M. Hosen *et al*., Observation of anisotropic Dirac cones in the topological material Ti_2Te_2P, Phys. Rev. B **106**, 125124 (2022).

[26] C.-K. Chiu and A. P. Schnyder, Classification of reflection-symmetry-protected topological semimetals and nodal superconductors, Phys. Rev. B **90**, 205136 (2014).

[27] B.-J. Yang, T. A. Bojesen, T. Morimoto, and A. Furusaki, Topological semimetals protected by off-centered symmetries in nonsymmorphic crystals, Phys. Rev. B **95**, 075135 (2017).

[28] Y. X. Zhao and A. P. Schnyder, Nonsymmorphic symmetry-required band crossings in topological semimetals, Phys. Rev. B **94**, 195109 (2016).

[29] B. J. Wieder and C. L. Kane, Spin-orbit semimetals in the layer groups, Phys. Rev. B **94**, 155108 (2016).

[30] L. M. Schoop, A. Topp, J. Lippmann, F. Orlandi, L. Müchler, M. G. Vergniory, Y. Sun, A. W. Rost, V. Duppel, M. Krivenkov *et al*., Tunable Weyl and Dirac states in the nonsymmorphic compound CeSbTe, Sci. Adv. **4**, eaar2317 (2018).

[31] A. A. Burkov, M. D. Hook, and L. Balents, Topological nodal semimetals, Phys. Rev. B **84**, 235126 (2011).

[32] A. Topp, R. Queiroz, A. Grüneis, L. Müchler, A. W. Rost, A. Varykhalov, D. Marchenko, M. Krivenkov, F. Rodolakis, J. L. McChesney *et al*., Surface floating 2D bands in layered nonsymmorphic semimetals: ZrSiS and related compounds, Phys. Rev. X **7**, 041073 (2017).

[33] M. M. Hosen, G. Dhakal, K. Dimitri, P. Maldonado, A. Aperis, F. Kabir, C. Sims, P. Riseborough, P. M. Oppeneer, D. Kaczorowski *et al*., Discovery of topological nodal-line fermionic phase in a magnetic material GdSbTe, Sci. Rep. **8**, 13283 (2018).

[34] N. Shumiya, J.-X. Yin, G. Chang, M. Yang, S. Mardanya, T.-R. Chang, H. Lin, M. S. Hossain, Y.-X. Jiang, T. A. Cochran *et al*., Evidence for electronic signature of a magnetic transition in the topological magnet HoSbTe, Phys. Rev. B **106**, 035151 (2022).

[35] S. Yue, Y. Qian, M. Yang, D. Geng, C. Yi, S. Kumar, K. Shimada, P. Cheng, L. Chen, Z. Wang *et al*., Topological electronic structure in the antiferromagnet HoSbTe, Phys. Rev. B **102**, 155109 (2020).

[36] B. Lv, J. Chen, L. Qiao, J. Ma, X. Yang, M. Li, M. Wang, Q. Tao, and Z.-A. Xu, Magnetic and transport properties of low-carrier-density Kondo semimetal CeSbTe, J. Phys.: Condens. Matter **31**, 355601 (2019).

[37] P. Li, B. Lv, Y. Fang, W. Guo, Z. Wu, Y. Wu, D. Shen, Y. Nie, L. Petaccia, C. Cao *et al*., Charge density wave and weak Kondo effect in a Dirac semimetal CeSbTe, Sci. China Phys. Mech. Astron. **64**, 237412 (2021).

[38] L. Y. Cao, M. Yang, L. Wang, Y. Li, B. X. Gao, L. Wang, J. L. Liu, A. F. Fang, Y. G. Shi, and R. Y. Chen, Optical study of the topological materials LnSbTe(Ln = La, Ce, Sm, Gd), Phys. Rev. B **106**, 245145 (2022).

[39] Y. Wang *et al*. Spectroscopic evidence for the realization of a genuine topological nodal-line semimetal in LaSbTe, Phys. Rev. B **103**, 125131 (2021).

[40] N. Valadez, I. Bin Elius, D. James, P. Radanovich, T. Romanova, S. Elgalal, G. Chajewski, F. Mesple, E. Thompson, K. T. Chu *et al*., Low-lying electronic structure of rare-earth based topological nodal line semimetal candidate DySbTe, arXiv:2503.15774.

[41] S. Regmi, R. Smith, A. P. Sakhya, M. Sprague, M. I. Mondal, I. B. Elius, N. Valadez, A. Ptok, D. Kaczorowski, and M. Neupane, Observation of gapless nodal-line states in NdSbTe, Phys. Rev. Mater. **7**, 044202 (2023).

[42] K. Pandey, R. Basnet, A. Wegner, G. Acharya, M. R. U. Nabi, J. Liu, J. Wang, Y. K. Takahashi, B. Da, and J. Hu, Electronic and magnetic properties of the topological semimetal candidate NdSbTe, Phys. Rev. B **101**, 235161 (2020).

[43] S. Regmi, G. Dhakal, F. C. Kabeer, N. Harrison, F. Kabir, A. P. Sakhya, K. Gofryk, D. Kaczorowski, P. M. Oppeneer, and M. Neupane, Observation of multiple nodal lines in SmSbTe, Phys. Rev. Mater. **6**, L031201 (2022).

[44] K. Pandey, D. Mondal, J. W. Villanova, J. Roll, R. Basnet, A. Wegner, G. Acharya, M. R. U. Nabi, B. Ghosh, J. Fujii *et al*., Magnetic topological semimetal phase with electronic correlation enhancement in SmSbTe, Adv. Quantum Technol. **4**, 2100063 (2021).

[45] S. Regmi, I. B. Elius, A. P. Sakhya, M. Sprague, M. I. Mondal, N. Valadez, V. Buturlim, K. Booth, T. Romanova, K. Gofryk *et al*., Electronic structure in a rare-earth based nodal-line semimetal candidate PrSbTe, Phys. Rev. Mater. **8**, L041201 (2024).

[46] I. Plokhikh, V. Pomjakushin, D. J. Gawryluk, O. Zaharko, and E. Pomjakushina, Competing magnetic phases in LnSbTe (Ln = Ho and Tb), Inorg. Chem. **61**, 11399 (2022).

[47] F. Gao, J. Huang, W. Ren, H. Wu, M. An, X. Wu, L. Zhang, T. Yang, A. Wang, Y. Chai *et al*., Magnetic and magnetotransport properties of the magnetic topological nodal-line semimetal TbSbTe, Adv. Quantum Technol. **6**, 2200163 (2023).

[48] K. Momma and F. Izumi, VESTA3 for three-dimensional visualization of crystal, volumetric and morphology data, J. Appl. Crystallogr. **44**, 1272 (2011).

[49] A. Kokalj, XCrySDen—A new program for displaying crystalline structures and electron densities, J. Mol. Graph. Model. **17**, 176 (1999).

[50] M. Neupane, M. M. Hosen, I. Belopolski, N. Wakeham, K. Dimitri, N. Dhakal, J.-X. Zhu, M. Z. Hasan, E. D. Bauer, and F. Ronning, Observation of Dirac-like semi-metallic phase in NdSb, J. Phys.: Condens. Matter **28**, 23LT02 (2016).

[51] See Supplemental Material for sample characterization, additional experimental ARPES results, and schematics, which contains Refs. [32,46,47,65].

[52] P. E. Blöchl, Projector augmented-wave method, Phys. Rev. B **50**, 17953 (1994).

[53] G. Kresse and J. Hafner, *Ab initio* molecular-dynamics simulation of the liquid-metal–amorphous-semiconductor transition in germanium, Phys. Rev. B **49**, 14251 (1994).

[54] G. Kresse, and J. Furthmüller, Efficient iterative schemes for *ab initio* total-energy calculations using a plane-wave basis set, Phys. Rev. B **54**, 11169 (1996).

[55] G. Kresse, and D. Joubert, From ultrasoft pseudopotentials to the projector augmented-wave method, Phys. Rev. B **59**, 1758 (1999).

[56] J. P. Perdew, K. Burke, and M. Ernzerhof, Generalized gradient approximation made simple, Phys. Rev. Lett. **77**, 3865 (1996).

[57] S. L. Dudarev, G. A. Botton, S. Y. Savrasov, C. J. Humphreys, and A. P. Sutton, Electron-energy-loss spectra and the structural stability of nickel oxide: An LSDA+U study, Phys. Rev. B **57**, 1505 (1998).

[58] H. J. Monkhorst and J. D. Pack, Special points for Brillouin-zone integrations, Phys. Rev. B **13**, 5188 (1976).

[59] N. Marzari, and D. Vanderbilt, Maximally localized generalized Wannier functions for composite energy bands, Phys. Rev. B **56**, 12847 (1997).

[60] I. Souza, N. Marzari, and D. Vanderbilt, Maximally localized Wannier functions for entangled energy bands, Phys. Rev. B **65**, 035109 (2001).

[61] N. Marzari, A. A. Mostofi, J. R. Yates, I. Souza, and D. Vanderbilt, Maximally localized Wannier functions: Theory and applications, Rev. Mod. Phys. **84**, 1419 (2012).

[62] G. Pizzi *et al*. WANNIER90 as a community code: New features and applications, J. Phys.: Condens. Matter **32**, 165902 (2020).

[63] M. P. L. Sancho, J. M. Lopez Sancho, J. M. L. Sancho, and J. Rubio, Highly convergent schemes for the calculation of bulk and surface Green functions, J. Phys. F: Met. Phys. **15**, 851 (1985).

[64] Q. S. Wu, S. N. Zhang, H.-F. Song, M. Troyer, and A. A. Soluyanov, WANNIERTOOLS: An open-source software package for novel topological materials, Comput. Phys. Commun. **224**, 405 (2018).

[65] I. Plokhikh, V. Pomjakushin, D. J. Gawryluk, O. Zaharko, and E. Pomjakushina, On the magnetic structures of 1:1:1 stoichiometric topological phases *Ln*SbTe ($Ln =$ Pr, Nd, Dy and Er), J. Magn. Magn. Mater. **583**, 171009 (2023).

[66] P. Gebauer, H. Poddig, L. T. Corredor-Bohorquez, T. V. Menshchikova, I. P. Rusinov, P. Golub, F. Caglieris, C. Benndorf, T. Lindemann, E. V. Chulkov *et al.*, Heavy-atom antiferromagnet GdBiTe: An interplay of magnetism and topology in a symmetry-protected topological semimetal, Chem. Mater. **33**, 2420 (2021).

[67] D. Yuan *et al.*, Observation of Dirac nodal line states in topological semimetal candidate PrSbTe, Phys. Rev. B **109**, 045113 (2024).